Morphological and Mechanical Characterization of P-Scaffolds with Different Porosity

Marta De Giorgi(✉), Nunzia Gallo, Marta Madaghiele, and Anna Eva Morabito

University of Salento, Lecce 73100, Italy
marta.degiorgi@unisalento.it

Abstract. The aim of this paper is to model and to compare the results of the mechanical characterization, carried out on numerical models and real specimens, of uniform P-scaffolds with different porosity values. The analysis includes the morphological characterization of 3D printed specimens and the implementation of a FEM shell model to reproduce a compressive test suitable for mechanical properties evaluation of PLA scaffolds. Young modulus and yield strength were also obtained, in order to verify the numerical model accuracy, by experimental tests on 3D printed PLA scaffolds. Numerical results showed that the shell model was able to reproduce, more efficiently compared to a solid model proposed in a previous work, both elastic and plastic behavior of the scaffolds, providing elastic modulus values very close to the experimental ones. On the other hand, the not very high quality of the 3D printing, detected by MicroCT analysis, caused a significant dispersion in the yield strength numerical values respect to the real data. Anyway, an inverse correlation between mechanical properties and porosity was found as expected. The elastic modulus values were similar to the typical values of the trabecular bone for whose regeneration this kind of scaffolds is usually employed.

Keywords: TPMS scaffold · MicroCT · FEM analysis · Experimental tests

1 Introduction

In recent years, tissue engineering has become a topic of great interest, emerging as suitable approach to replace and regenerate damaged and/or diseased tissue. In the case of tissues designed for making bone substitutes with predominantly biomechanical functions, however, several open issues remain. The load-bearing scaffolds do not often promote a successful tissue ingrowth or the complete scaffold integration in the host tissue. Sometimes, the mechanical properties of the scaffold are not similar to those of the surrounding bone and these mismatches can affect the operation or longevity of the implant, because of the effect known as stress shielding [1].

In the design of load-bearing structures for the bone tissue regeneration, the aspects to be considered are numerous and concern the shape of the bone defect and the performances required to the scaffold in terms of mechanical, fluid-dynamic, and cellular proliferation properties. Thanks to the Additive Manufacturing (AM), it is now

C. Rizzi et al. (Eds.): ADM 2019, LNME, pp. 361–372, 2020.
https://doi.org/10.1007/978-3-030-31154-4_31

possible to manufacture porous bone substitutes with complex geometry able to reproduce perfectly bone defect shapes [2]. In order to promote the cellular proliferation and transport of nutrients, an appropriate porous structure with interconnected porosity has to be designed. Given the pivotal role that nutrients flow plays in promoting cellular proliferation and differentiation, the scaffold surface must be characterized by high values of permeability that is a parameter related to geometrical characteristics such as pore shape and size. High-values of surface to volume ratio are also beneficial in order to allow large number of cells to attach and migrate into porous scaffolds [3]. Furthermore, it was shown that curved surfaces can promote cell proliferation more than lattice-based architectures and, recently, a correlation between support curvature and tissue regeneration was found in [4], which points out that concave surfaces are preferable to convex and flat surfaces.

Several are the methodologies available to model these structures; some examples are: CAD-based methods [5, 6], Image-based methods (MRI/CT) [7] and topology optimization [8]. Recently, methods for the optimization of scaffolds microstructure geometry, based on mechano-biological criteria, have been also proposed [9].

Triply periodic minimal surfaces (TPMS) are very attractive candidates for the design of biomorphic porous scaffolds. This interest is justified by the several natural manifestations that these surfaces show, such as biological structures, block copolymers and equipotential surfaces in crystals [10]. Moreover, most TPMS forms exist as an interface between two phases [11]. From a mathematical point of view, TPMS are surfaces periodic along three directions mutually perpendicular between each other and with zero mean curvature at each point. Different are the surfaces attributable to this class that are often considered for scaffold design [12]. For the TPMS modelling, the approach based on a single implicit function (called implicit surface modelling, ISM) is very suitable [13].

Scaffolds, based on these surfaces, have shown to provide high values of permeability [14] and their curved configuration can promote cellular proliferation more than scaffold architectures based on lattice cells [15]. While, on the one hand, high values of porosity and large pore sizes favor nutrients flow and cell ingrowth, on the other they can limit the load bearing capability of the scaffold. Therefore, when designing these structures, a compromise has to be found between biological and mechanical requirements, which means that the ideal material for scaffold fabrication should satisfy specific criteria. It must be biocompatible and capable to reproduce the network architecture of the natural bone in order to create a microenvironment stimulating cell attachment. The design of temporary scaffolds, as polymeric scaffolds, moreover, must ensure the compatibility of degradation products, the rate of the degradation process and how each of these affects the regenerative process. The degradation phenomenon affects the mechanical properties of the scaffold. On the other hand, the use of degradable polymers is required if the surgical removal must be avoided. A slow degradation process allows maintaining the scaffold mechanical properties up to the regenerative process is in an advanced stage. On the basis of these premises, the most usually used degradable synthetic polymer is the FDA-approved poly(lactic acid) (PLA) because the rate of degradation can be tuned by composition obtaining time of degradation from months to several years [16–18]. Due to the availability, biocompatibility, and processibility, PLA is used for 3D culture and transplantation of

articular, auricular, nasal, costochondral, tracheal, and intervertebral disk cartilage cells [19]. PLA is also recommended for bone fixing after a cancellous bone fracture, osteotomy, or arthrodesis/joint fusion. PLA is also a material suitable for 3D printing that allows the fabrication of complex, multiscale structures through computer-aided design (CAD) [20–24].

In the adult human skeleton, the cortical bone represents the 80% of the skeletal mass and performs the supportive and protective function. The cortical bone constitutes the external wall of all bones. It shows a solid mass with microscopic channels (Fig. 1). The internal portion of bones, i.e. the remaining 20% of the bone mass, is formed by trabecula and it is called cancellous bone (Fig. 1). Large difference exists in the cortical and cancellous distribution depending on bone type. The ulna, for example, consists of 92% cortical and 8% cancellous bone, while a vertebra presents a 62% cortical and 38% cancellous bone [25].

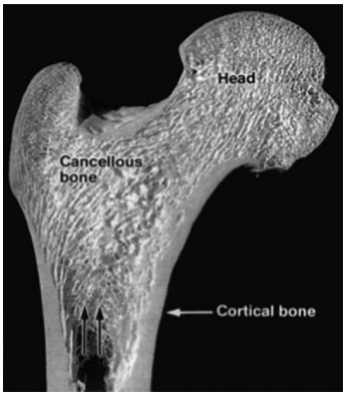

Fig. 1. Example of bone composition: cortical and cancellous region [25].

The more suitable test to determine the mechanical properties of a bone mainly depends on the kind of bone being tested (cortical or trabecular bone), the age of the bone and its location in the skeleton. In the case of cortical bones, the bending test should be performed, while in the case of the trabecular bone, the compression test is suggested. The compression test is usually performed to evaluate the biomechanical properties of the trabecular bone, which is present in large quantities in the vertebrae [26]. In the vertebrae, in fact, compressive tests reproduce the in vivo loading conditions to which the bone is subjected. The structural properties depend on the cancellous bone density and trabecular orientation. As reported in literature [19, 26], the Young's modulus in the cancellous bone can vary from 0.1 to 4.5 GPa.

In this paper, PLA scaffolds having different porosity were characterized, in terms of compressive mechanical properties, from a numerical and experimental point of view. The surface model of a cubic scaffold, generated by an original MATLAB routine, was used as input in order to implement the FEM model as shell model. This solution allowed overcoming the significant difficulties encountered in a previous work [27]

where a solid FEM model was considered. Several problems associated to the data exchange between different s/w were avoided and laborious manual operations for mesh correction were eliminated using a shell model. By adopting this modelling strategy, several scaffold models having different morphological properties can be evaluated fast and efficiently. The above-mentioned geometric model was also used for 3D printing of PLA specimens to be subjected to the compressive test. Moreover, a deep morphological characterization was performed through a micro-tomographic analysis on the printed specimen, in order to evaluate, by the comparison of a set of specific cell properties, its deviations from the nominal geometry.

2 Materials and Methods

2.1 P-Scaffold Modelling

Scaffolds for bone tissue regeneration can be obtained by replicating a single TPMS cell along the three orthogonal directions or by combining TPMS cells with different geometrical configuration in order to obtain graded porosity scaffolds. Among the various TPMS, the Schwarz's Primitive minimal surface (hereinafter referred as P-surface) has been considered in this study. The P-surface can be described, to the first order of approximation, by the following nodal equation:

$$f(x, y, z, s, k) = \cos(x/s) + \cos(y/s) + \cos(z/s) - k \quad (1)$$

under the boundary conditions $x = [-\pi, \pi]$, $y = [-\pi, \pi]$ and $z = [-\pi, \pi]$. A detailed description of the P-cell can be found in a previous work [28].

In this paper, the implicit function for a P-surface with $s = 1$ and $k = 0$ was considered to model, by an original MATLAB routine, a cubic scaffold with a number N of cells along the side equal to 7. The unit cell presented a length of side L equal to 2π mm. This model is given in the form of a tessellated model described by a .stl file and presents 117992 faces and 59976 vertices (Fig. 2).

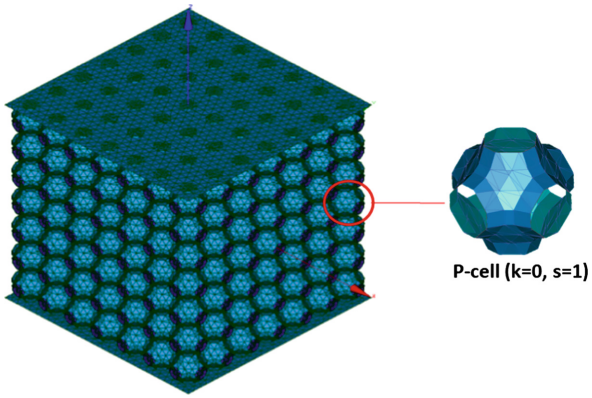

Fig. 2. Tessellated cubic scaffold and detail of the unit cell with $L = 2\pi$ and $N = 7$.

2.2 Experimental Characterization of P-Scaffold

In this work, experimental data used for comparison with numerical models were obtained through compressive tests. The uniaxial compression test is the easiest and most efficacious way to determine the mechanical behaviour of porous structures under static conditions and it is the recommended test for cancellous bone characterization [26, 29, 30]. Therefore, the stress-strain compressive curve is assumed as the term of comparison to evaluate the numerical model reliability.

Nine specimens having three different porosity values of the cubic scaffold were manufactured by the 3D printer Ultimaker 2.0. In particular, scaffolds having nominal porosity equal to 88, 82 and 76% were modeled and realized assigning a thickness t of 0.4, 0.6 and 0.8 mm to the cell wall respectively. The nominal values of porosity were calculated on the solid cell obtained in Meshlab through an offset operation on the tessellated surface of Fig. 2. The PLA filament with 2.85 mm diameter was extruded at an optimal temperature of 210 °C using 0.4, 0.6 and 0.8 mm nozzle for 0.4, 0.6 and 0.8 mm cell wall thickness respectively. The print speed and the layer thickness were set to 40 mm/s and 0.1 mm respectively using a flow equal to 100%.

The 3D structure of the printed scaffolds was assessed by microcomputed tomography (Bruker Skyscan 1172, Kontich, Belgium). Three samples, one for each porosity value, were scanned at a nominal resolution of 26.8 μm, with a camera pixel binning of 4 × 4. The X-ray source was set at 50 kV and 200 μA, and no filter was used. The scan orbit was 180°, with a rotation step of 0.3°. Camera offset was applied to scan the entire cross-section of the samples having 5 cells for side (31.42 × 31.42 mm), while the scanned height was about 16 mm. After reconstruction with NRecon software, DataViewer software was used to visualize the sections of the scaffolds in the XY, XZ and YZ planes. The reconstructed grey scale images of the XY sections were then analyzed with CTAn software to quantify the porosity and the average thickness of the pore walls, after selection of the volume of interest (VOI) and appropriate thresholding. Two VOIs were analyzed to compare the structure of the printed scaffolds with that of the original .stl models, respectively a unit cube (6.28 × 6.28 × 6.28 mm) corresponding to the single P-cell (taken at the center of the scanned sample) and a square prism (31.5 × 31.5 × 16 mm) enclosing the overall cross-section of the scaffolds.

Compression tests were carried out on a servo-hydraulic MTS 810 machine having 100 kN load capacity equipped with two planar plates (Fig. 3), according to the ASTM D 1621-00 Standard [31]. The crosshead speed was fixed at 4 mm/min. Strain was calculated dividing the cross-head displacement by the cubic specimen side approximately equal to 44 mm. Three specimens for each cell wall thickness t were tested. Moreover, in order to characterize the mechanical behavior of PLA base material, three bulk specimens 20 × 20 × 20 mm were tested.

2.3 FEM Analysis

Numerical analysis was performed using the open source FEM software Code-Aster R13.6. A discretization in triangular shell elements, named DKT and having a linear formulation, was in particular adopted. The models consisted of 75308 elements and 36668 nodes and they differed for the value of the cell wall thickness t (0.4, 0.6 and 0.8 mm). The study was performed in the large displacements range. An isotropic elastic-perfectly plastic stress-strain behaviour of the material was, in particular, hypothesized. The material properties, required by the numerical analysis, were obtained as the average of the mechanical properties resulting from the compressive tests carried out on the bulk specimens. Boundary conditions were applied on the lower face, imposing a zero value to z-direction displacement and rigid body boundaries; the load was applied to the upper surface as a 10 MPa pressure load distributed in 100 substeps to overcome convergence troubles. Figure 2 shows the mesh of the FEM model.

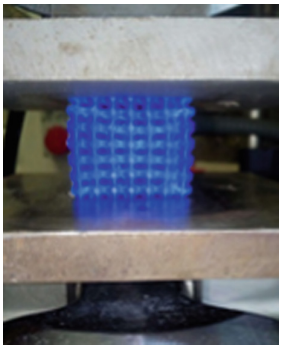

Fig. 3. Example of specimen under compression.

3 Results and Discussions

3.1 MicroComputed Tomography (MicroCT)

As shown in Fig. 4, MicroCT scanning of printed samples confirmed the highly interconnected porosity of the scaffolds and the different thickness of their pore walls, the latter in rough agreement with the values set for the printing. Quantitative 3D analysis evidenced an overall porosity of 87.4%, 84.2% and 79.9% for PLA04, PLA06 and PLA08 samples, respectively, which is consistent with the increasing pore wall thickness and with the values of porosity evaluated from the tessellated nominal models obtained applying the thickness t to the scaffold surface of Fig. 2.

Porosity was mostly open, as expected, due to the high interconnectivity of the P-cells. However, a certain amount of closed porosity was also detected, which was found to increase when the pore wall thickness was increased (0.013%, 0.108% and 0.331% of closed porosity for PLA04, PLA06 and PLA08, respectively). Closed porosity indicated the presence of a certain number of voids (air bubbles) in the cell

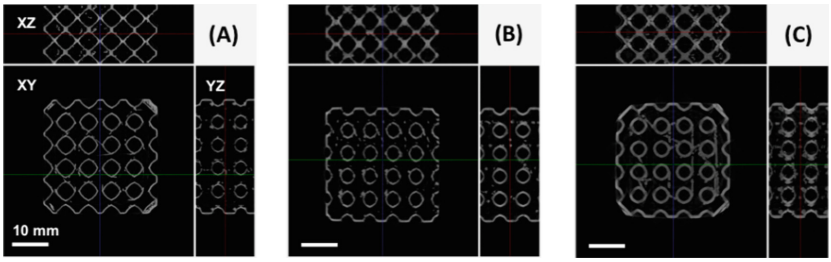

Fig. 4. Representative cross-sections of the PLA scaffolds, obtained from MicroCT analysis: (A) PLA04, (B) PLA06 and (C) PLA08.

walls. Furthermore, the average structure thickness of the scaffolds was found to be lower than the theoretical set values (0.4, 0.6 and 0.8 mm), and in particular was found the values in Table 1. Overall, these observations suggested that the printing accuracy was greatly reduced when increasing the theoretical thickness of the deposited material. This was also confirmed by the presence of a large amount of undesired material within the porous cells, for PLA06 and PLA08 samples, in the form of filaments that the

Table 1. Characteristics of the porous specimens and experimental mechanical data (nom stands for nominal and act for actual).

Specimen	t_{nom} [mm]	t_{act} [mm]	P_{nom} [%]	P_{act} [%]	E_{exp} [MPa]	σ_{y_exp} [MPa]	E_{num} [MPa]	σ_{y_num} [MPa]	$Error_E$ [%]	$Error_{\sigma y}$ [%]
P1_0.4		0.35		87	34	0.9				
P2_0.4	0.4	± 0.125	88		38	1.0	39	2.7	3	170
P3_0.4					43	1.0				
P1_0.6		0.45		84	75	2.2				
P2_0.6	0.6	± 0.167	82		80	2.3	69	4.0	13	82
P3_0.6					83	2.2				
P1_0.8		0.50		80	131	3.9				
P2_0.8	0.8	± 0.229	76		108	2.8	108	5.8	16	61
P3_0.8					147	4.1				

nozzle leaves during its translation (Fig. 4). When analyzing the cubic VOI of a single P-cell and visualizing the corresponding .stl model, unexpected holes were also found through the cell wall, and these irregularities were more evident for PLA06 and PLA08 samples with respect to PLA04 one (Fig. 5).

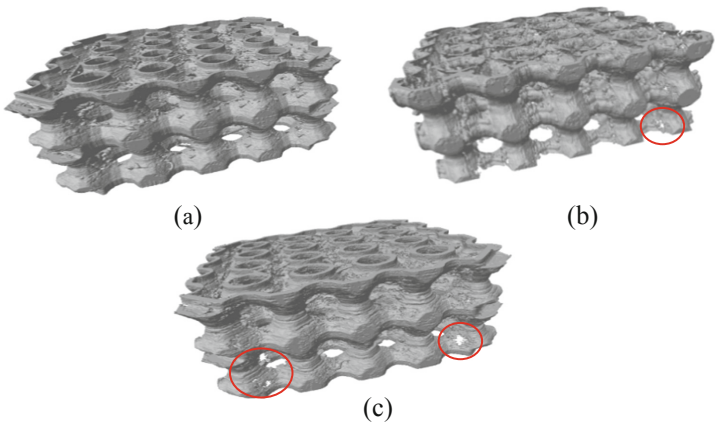

Fig. 5. 3D visualization from μ-CT analysis for 0.4 (a), 0.6 (b) and 0.8 (c) mm cell wall thickness.

3.2 Numerical and Experimental Mechanical Characterization

Three preliminary compression tests were performed on bulk specimens in order to evaluate the mechanical properties of PLA printed material. Compression curve is reported as example in Fig. 6a. The resulting Young modulus and yield strength, used as inputs in the FEM analysis, were 1280 MPA and 67 MPa respectively. Stress-strain curves, deduced from the experimental tests on P-scaffolds, were similar to those reported in literature for bone (Fig. 6b) [26, 32]. The yield point is an imaginary boundary, above which stresses cause permanent damage (plastic deformation) to the bone structure. The last phase, represented by the rapid load increase, is due to the specimen densification.

The remaining compressive tests were carried out on three scaffolds for each cell wall thickness. Table 1 reports the characteristics of the specimens and the resulting mechanical data. These values were used to evaluate the reliability of the FEM models, whose results, in term of displacement, are shown in Fig. 7 for the model with the highest porosity and at a load corresponding to 1, 2 and 3 MPa. Note that 3 MPa represented, in this case, a stress level slightly higher than yield strength estimated for the numerical scaffold.

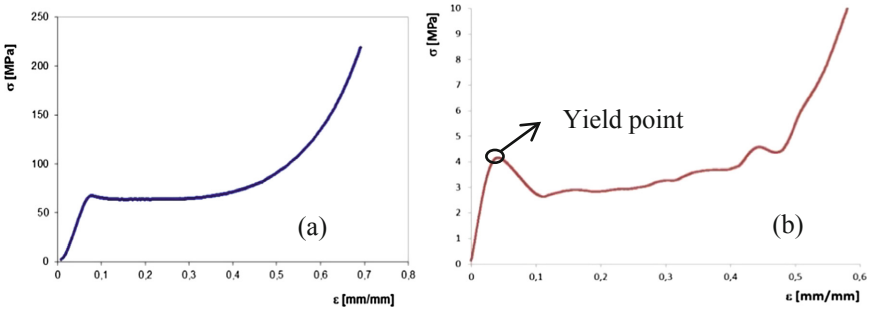

Fig. 6. Compression curves of the bulk specimen (a) and 3D printed scaffold (b).

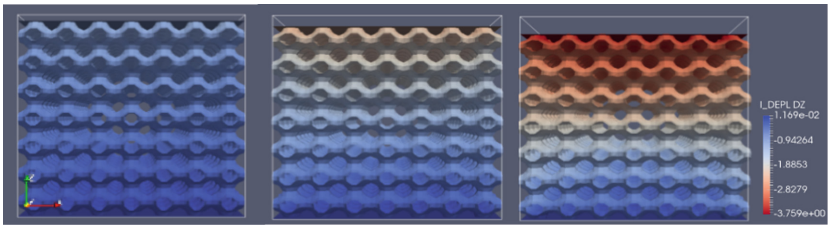

Fig. 7. Maps of displacements at the load of 1, 2 and 3 MPa for the most porous P-scaffold.

The ratio of upper surface displacement to cubic model side allowed calculating the global strain of the scaffold. The stress-strain curves are reported in Fig. 8 in comparison with experimental curves.

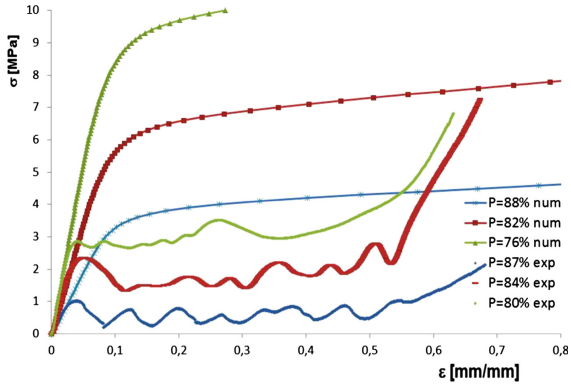

Fig. 8. Experimental and numerical stress-strain curves for different porosity values.

Figure 9 shows the detail of the linear portion of the experimental and numerical compression curves.

The first evident result is that the numerical model is able to predict the elastic behavior of the scaffold with high accuracy. The error in the Young modulus prediction is significantly lower than 20% as reported in Table 1. As regards to the plastic behavior, the model is also adequate to reproduce the plastic phase but with a higher error in the yield strength prediction. This is due to the microplasticizations that actually occur at the interface between two cells and to the buckling of the cell walls. In fact, it can be seen that the error increases for lower cell wall thickness that is responsible of higher plasticization and lower buckling strength. These phenomena are not considered in the present analysis. Moreover, the real foam structure obtained from the 3D printing is not defects free, as demonstrated from the MicroCT analysis and visible in Fig. 5. This causes lower strength at loads over yield point. A significant improvement on numerical model can be achieved also considering for the base material a damage model suitable for porous structures. In particular, the Gurson-Tvergaard-Needleman (GTN) damage

law is able to explain the local strength decrease [33, 34]. The GTN damage model has been implemented in the last version of the Code-Aster FEM software and it will be taken in account in the future numerical analysis.

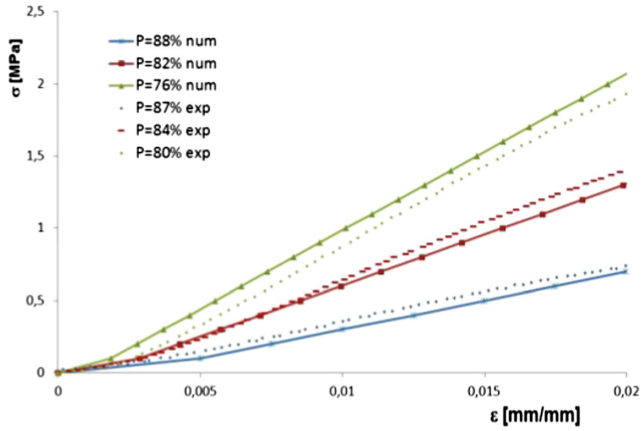

Fig. 9. Linear portion of compression curves: comparison between numerical and experimental results for different porosity values.

4 Conclusions

The shell model of the P-scaffold implemented here allowed overcoming some significant difficulties encountered during the data exchange pertaining to the solid model proposed in a previous work [27]. Several laborious manual operations for mesh correction were eliminated. A morphological and mechanical characterization on uniform P-scaffolds with different porosity has been performed. MicroCT analysis revealed a real structure of the scaffold coherent with the geometrical model but not defect free. Closed micro-porosities and holes through the cell walls were the principal cause of the different compressive behaviour in the plastic region between FEM models and real specimens. The micro-plasticizations that actually occur at the interface between two cells and the buckling of the cell walls were amplified because of the defects in the cell walls, particularly in the scaffold with lowest cell wall thickness. On the other hand, the shell FEM model simulated the elastic behaviour of this complex structure very well providing elastic modulus values comparable with those of cancellous bones. Moreover, an inverse correlation between mechanical properties and porosity was found as expected. A significant improvement of the numerical model can be achieved using as input the real geometric model obtained by MicroCT and considering a damage model suitable for porous structures, as the Gurson-Tvergaard-Needleman (GTN) damage law. Results obtained on the shell model will be compared

with data resulting from the solid model implemented in [27], assigning to this last one the PLA mechanical properties. Moreover, graded porosity scaffolds, i.e. structures where pore architecture varies throughout the scaffold, will be analyzed too. These scaffolds are of particular interest, since they are more similar to the stochastic configuration of real bone [35].

References

1. Gao, W., Zhang, Y., Ramanujana, D., Ramani, K., Chen, Y., Williams, C.B., Wang, C.C., Shin, Y.C., Zhang, S., Zavattieri, P.D.: The status, challenges, and future of additive manufacturing in Engineering. Comput.-Aided Des. **69**, 65–89 (2015)
2. Do, A.V., Smith, R., Acri, T.M., Geary, S.M., Salem, A.K.: 9 − 3D printing technologies for 3D scaffold engineering. Funct. 3D Tissue Eng. Scaffolds, 203–234(2018)
3. Lanza, R., Langer, R., Vacanti, J.P.: Principles of Tissue Engineering, 1344 p. Academic Press, Cambridge (2011)
4. Park, J.Y., Lee, D.H., Lee, E.J., Lee, S.-H.: Study of cellular behaviors on concave and convex microstructures fabricated from elastic PDMS membranes. Lab Chip **9**(14), 2043–2049 (2009)
5. Chantarapanich, N., Puttawibul, P., Sucharitpwatskul, S., Jeamwatthanachai, P., Inglam, S., Sitthiseripratip, K.: Scaffold Library for Tissue Engineering: A Geometric Evaluation. Comput. Math. Methods Med. vol. 2012, 14 p (2012). Article ID07805
6. Carofalo, A., De Giorgi, M., Morabito, A.E.: Geometric modelling of metallic foams. Eng. Comput. **30**(7), 924–935 (2013)
7. Hollister, S.J., Maddox, R.D., Taboas, J.M.: Optimal design and fabrication of scaffolds to mimic tissue properties and satisfy biological constraints. Biomaterials **23**, 4095–4103 (2002)
8. Wang, X., Xu, S., Zhou, S., Xu, W., Leary, M., Choong, P., Qian, M., Brandt, M., Min, Xie Y.: Topological design and additive manufacturing of porous metals for bone scaffolds and orthopaedic implants: a review. Biomaterials **83**, 127–141 (2016)
9. Boccaccio, A., Uva, A.E., Fiorentino, M., Lamberti, L., Monno, G.: A mechanobiology-based algorithm to optimize the microstructure geometry of bone tissue scaffolds. Int. J. Biol. Sci. **12**, 1–17 (2016)
10. Lord, E.A., Mackay, A.L.: Periodic minimal surfaces of cubic symmetry. Curr. Sci. **85**(3), 346–362 (2003)
11. Han, S.C., Choi, J.M., Liu, G., Kang, K.: A microscopic shell structure with Schwarz's D-Surface. Sci. Rep. **7**, 13405 (2017)
12. Yan, C., Hao, L., Hussein, A., Young, P.: Ti-6Al-4 V triply periodic minimal surface structures for bone implants fabricated via selective laser melting. J. Mech. Behav. Biomed. Mater. **51**, 61–73 (2015)
13. Gabbrielli R., Turner I.G., Bowen C.R.: Development of modelling methods for materials to be used as bone substitutes. In: Daculsi, G., Layrolle, P (Eds) Key Engineering Materials, vol. 361–363, pp. 903–906. Scientific.net Zurich (2008)
14. Zhang, Z., Jones, D., Yue, S., Lee, P.D., Jones, J.R., Sutcliffe, C.J., Jones, E.: Hierarchical tailoring of strut architecture to control permeability of additive manufactured titanium implants. Mater. Sci. Eng. C **33**, 4055–4062 (2013)
15. Rajagopalan, S., Robb, R.A.: Schwarz meets Schwann: Design and fabrication of biomorphic and durataxic tissue engineering scaffolds. Med. Image Anal. **10**, 693–712 (2006)

16. Shoichet, M.S.: Polymer scaffolds for biomaterials applications. Macromolecules **43**(5), 581–591 (2010)
17. Sultana, N., Wang, M.: Fabrication of HA/PHBV composite scaffolds through the emulsion freezing/freeze-drying process and characterisation of the scaffolds. J. Mater. Sci. Mater. Med. **19**, 2555–2561 (2008)
18. Zhang, T., Zhou, S., Gao, X., Yang, Z., Sun, L., Zhang, D.: A multi-scale method for modelling degradation of bioresorbable polyesters. Acta Biomater. **50**, 462–475 (2017)
19. Moran, J.M., Pazzano, D., Bonassar, L.J.: Characterization of polylactic acid polyglycolic acid composites for cartilage tissue engineering. Tissue Eng. **9**, 63–70 (2003)
20. Kucharska, M., Butruk, B., Walenko, K., Brynk, T., Ciach, T.: Fabrication of in-situ foamed chitosan/β-TCP scaffolds for bone tissue engineering application. Mater. Lett. **85**, 124–127 (2012)
21. Fayyazbakhsh, F., Solati-Hashjin, M., Keshtkar, A., Shokrgoza, M.A., Dehghan, M.M., Larijani, B.: Novel layered double hydroxideshydroxyapatite/gelatin bone tissue engineering scaffolds: fabrication, characterization, and in vivo study. Mater. Sci. Eng., C **76**, 701–714 (2017)
22. Cao, H., Kuboyama, N.: A biodegradable porous composite scaffold of PGA/β-TCP for bone tissue engineering. Bone **46**(2), 386–395 (2010)
23. Cui, L., Zhang, N., Cui, W., Zhang, P., Chen, X.: A novel nano/micro-fibrous scaffold by melt-spinning method for bone tissue engineering. J. Bionic Eng. **12**(1), 117–128 (2015)
24. Sanatgar, R.H., Campagne, C., Nierstrasz, V.: Investigation of the adhesion properties of direct 3D printing of polymers and nanocomposites on textiles: effect of FDM printing process parameters. Appl. Surf. Sci. **403**, 551–563 (2017)
25. Cowin, S.C.: Bone Mechanics, 2nd edn. CRC Press, Boca Raton (2001)
26. Disease, K., Oksztulska-Kolanek, E., Znorko, Małgorzata B., Pawlak, M.K.: Nephron **132**, 51–58 (2016)
27 Ambu, R., Morabito, A.E.: Design and analysis of tissue engineering scaffolds based on open porous non-stochastic cells. Lecture Notes in Mechanical Engineering, pp. 777–787 (2017). Springer, Cham
28. Ambu, R., Morabito, A.E.: Modeling, assessment, and design of porous cells based on schwartz primitive surface for bone scaffolds. Sci. World J. 2019, Article ID 7060847, 16 p (2019). https://doi.org/10.1155/2019/7060847
29. Turner, C.H., Burr, D.B.: Basic biomechanical measurements of bone a tutorial. Bone **14**(4), 595–608 (1993)
30. Turner, C.H., Cowin, S.C., Rho, J.Y., Ashman, R.B., Rice, J.C.: The fabric dependence of the orthotropic elastic constants of cancellous bone. J. Biomech. **23**, 549–561 (1990)
31. ASTM D1621-16, Standard Test Method for Compressive Properties of Rigid Cellular Plastics, ASTM International, West Conshohocken, PA (2016)
32. Mercer, C., He, M.Y., Wang, R., Evans, A.G.: Mechanisms governing the inelastic deformation of cortical bone and application to trabecular bone. Acta Biomater. **2**, 59–68 (2006)
33. Cricrì, G.: Consistent use of the Gurson-Tvergaard damage model for the R-curve calculation. In: Proceedings of IGF XX, Torino, pp. 138-150, 24–26 June 2009
34. Gurson, A.L.: Continuum Theory of ductile rupture by void nucleation and growth – Part I. Yield criteria and flow rules for porous ductile media. J. Engrg. Mat. Tech. **99**, 2–15 (1977)
35. Ambu, R., Morabito, A.E.: Porous scaffold design based on minimal surfaces: Development and assessment of variable architectures. Symmetry **10**(9), 361 (2018)